BMC Oral Health

RESEARCH Open Access

On the osteogenic differentiation of dental pulp stem cells by a fabricated porous nano-hydroxyapatite substrate loaded with sodium fluoride

Samaneh Arab[1], Marjan Bahraminasab[1*], Samira Asgharzade[2,3], Ali Doostmohammadi[4], Zahra Khatib Zadeh[4] and Vajihe Taghdiri Nooshabadi[1]

Abstract

In the present study, nano-hydroxyapatite (n-HA) powder was extracted from carp bone waste to fabricate porous n-HA substrates by a molding and sintering process. Subsequently, the substrates were loaded with different amounts of sodium fluoride (NaF) through immersion in NaF suspensions for 10, 7.5, and 5 min. The NaF-loaded n-HA substrates were then examined for their structural and physical properties, chemical bonds, loading and release profile, pH changes, cytotoxicity, and osteogenic effect on dental pulp stem cells (DPSCs) at the level of RNA and protein expression. The results showed that the n-HA substrates were porous (>40% porosity) and had rough surfaces. The NaF could be successfully loaded on the substrates, which was 6.43, 4.50, and 1.47 mg, respectively for n-HA substrates with immersion times of 10, 7.5, and 5 min in the NaF suspensions. It was observed that the NaF release rate was rather fast during the first 24 h in all groups (39.06%, 36.43%, and 39.57% for 10, 7.5, and 5 min, respectively), and decreased dramatically after that, indicating a slow detachment of NaF. Furthermore, the pH of the medium related to all materials was changed during the first 4 days of immersion (from 7.38 to pH of about 7.85, 7.84, 7.63, and 7.66 for C0, C5, C7.5, and C10, respectively). The pH of media associated with the C7.5, and C10 increased up to 4 days and remained relatively constant until day 14 (pH = 7.6). The results of the cytotoxicity assay rejected any toxicity of the fabricated NaF-loaded n-HA substrates on DPSCs, and the cells could adhere to their surfaces with enlarged morphology. The results showed no effect on the osteogenic differentiation at the protein level. Nevertheless, this effect was observed at the gene level.

Keywords Nano-hydroxyapatite, Sodium fluoride, Tissue engineering, Dental pulp, Stem cells

*Correspondence:
Marjan Bahraminasab
m.bahraminasab@yahoo.com
[1]Department of Tissue Engineering and Applied Cell Sciences, School of Medicine, Semnan University of Medical Sciences, Semnan, Iran
[2]Cellular and Molecular Research Center, Basic Health Sciences Institute, Shahrekord University of Medical Sciences, Shahrekord, Iran
[3]Department of Molecular Medicine, School of Advanced Technologies, Shahrekord University of Medical Sciences, Shahrekord, Iran
[4]Student Research Committee, Semnan University of Medical Sciences, Semnan, Iran

Introduction

Dental implants along with bone grafts are now often utilized in the oral and maxillofacial area to support prostheses at the site. Autografts are among the most successful types of bone grafts, but they need simultaneous surgery at the harvest site and are limited to small size defects. Moreover, the complications occurred for the recipient of the grafts after surgery are an additional problem in this type of grafting [1]. Nowadays, tissue engineering (TE) and bone regeneration techniques have evolved and are promising for the healing of jaw anomalies and the regeneration of masticatory teeth [2–6]. The bone substitutes offered by TE can be very effective, especially for critical size defects where the bone or tissue is unable to fully regenerate.

For fifty years, research has been carried out into replacing missing tissues with biomaterials. The nonfunctional or lost tissues are replaced with specific materials in order to restore the structural and functional properties. Tissue engineering can be used to treat abnormalities in the mouth, replace missing skin or oral structures and change a patient's smile. TE components, i.e. cells, biomaterials and physiologically active molecules, are also used to improve bone and tooth function and the long-term durability of implants [7, 8]. The aim of tissue regeneration using cell therapy, particularly stem cells, is to alter, regenerate or improve the biological patterns of injured tissue [9]. Biomaterials are used to make scaffolds, which are three-dimensional (3D) substrates and serve as templates for tissue regeneration by providing 3D biological and physicochemical environments to promote cell adhesion, growth, differentiation, and migration [10]. The scaffolds should ideally be able to transfer nutrients, oxygen, and excretory substances [11]. In addition, the scaffold materials should be non-toxic, and biocompatible with suitable mechanical strength, and the possibility of biodegradation and replacement with new tissue [12–14]. While it is possible to control physicochemical properties such as degradability rates in synthetic polymers, their degradation products (such as acidic polyester products) can have adverse biological effects [15, 16]. Ceramic materials are also used to make hard tissue scaffolds [17], one of which is hydroxyapatite (HA). About 70% of bones, 96% of enamel, 70% of dentin, and 45% of cementum are made up of HA nanocrystals [18, 19]. Hydroxyapatite is a biocompatible and bioactive material with suitable mechanical properties [20]. Furthermore, HA nanoparticles (n-HA) are one of the most biocompatible and bioactive materials that play an important role in various biomedical applications (both medicine and dentistry) [21–25]. This is due to its exceptional properties, such as its high surface-to-volume ratio and resemblance to biological HA, which has a great influence on the interaction of cells and biomaterials. The n-HA can be employed in the form of powder, dense, or porous blocks. This material is mainly used to treat periodontal defects, alveolar ridge augmentation, and mandibular injuries [23, 26]. Research has also shown that nano-hydroxyapatite has a high potential for tooth restoration [21, 27].

Certain substances, including sodium fluoride (NaF), aid in the mineralization of hard tissues, because of the ossifying properties [28]. NaF is frequently used in dental treatments, and it is considered a main drug to strengthen bone formation in patients with osteoporosis. It has been shown that the insertion of NaF to the culture medium of dental pulp stem cells (DPSCs) stimulates the expression of bone- and tooth-specific genes including runt-related transcription factor 2 (Runx2), dentin sialophosphoprotein (DSPP), osteocalcin (OSC), and bone morphogenetic protein 2 (BMP2) [9]. Furthermore, NaF has been also shown to stimulate the proliferation and differentiation of osteoblasts (MC3T3-E1) [29]. However, it should be pointed out that fluoride may have toxic effects on the body by affecting cellular metabolism and interfering with the function of some enzymes, while at the same time, it stimulates the activity of the other enzymes [30].

In this study, sodium fluoride is used as an effective auxiliary component to impregnate the porous n-HA substrates through a dip-coating approach. The hypothesis is that the NaF-loaded nano-hydroxyapatite substrates have a continuous and slow NaF release in situ, leading to improved growth and differentiation of DPSCs without cytotoxic effect. The positive effects of sodium fluoride on dental pulp cells have already been demonstrated. However, due to the toxicity of sodium fluoride in high concentrations, sustained drug release of this substance is very important. Therefore, the aim of the present study was to load NaF on porous nano-hydroxyapatite substrates, in which it acts as an inseparable component to achieve a sustained release, and to demonstrate its effects on the proliferation and osteogenic differentiation of DPSCs. With this method, we can approach to a ready-to-use product that in practice merely requires to be implanted in the defect site, without any additional work to be done by the practitioners.

Methods and materials

HA powder preparation

After collecting the carp bones, they were boiled in water for about 90 min to remove the fats attached to them. Then, they were air-dried, completely. Subsequently, they were crushed and placed in an electric furnace to sinter at 700 °C for 5 h [18]. To confirm the formed phases in the powder, x-ray diffraction (XRD) analysis was done (Bruker, D8-advance). Afterward, to obtain uniform nanoparticles, HA powder was ball-milled with a Teflon

cup and tungsten balls for 2 h using a planetary ball mill machine (Amin Asia, Iran). The rotation speed was 400 rpm with ball to powder ratio of 20:1. Scanning electron microscopy (SEM) images of the HA powder were provided to analyze the morphology and size of HA powders after ball mill using MIRA3, TESCAN.

NaF powder

Sodium fluoride powder was purchased from SIGMA-ALDRICH, Germany with a molecular weight of 41.99 g/mol and purity of >99%. XRD analysis (Bruker, D8-advance) of the powder was done in the 2θ range of 10–80°.

n-HA substrate preparation and loading of NaF

To prepare disc-shaped substrates, after mixing the powder and the biner, a sintering process was employed [31–33]. To do this, a 5% polyvinyl alcohol (PVA) solution was prepared as a binder. Then, n-HA powder was mixed with PVA, poured into a special 3D-printed plastic mold (mold cavity diameter was 7 mm), and compressed. After removing the samples from the mold, they were sintered in an electric furnace at 300 ° C for one hour, then the temperature was raised to 1100 ° C and remained for one hour. Figure 1a and b show the mold components and the procedure used to make n-HA substrates.

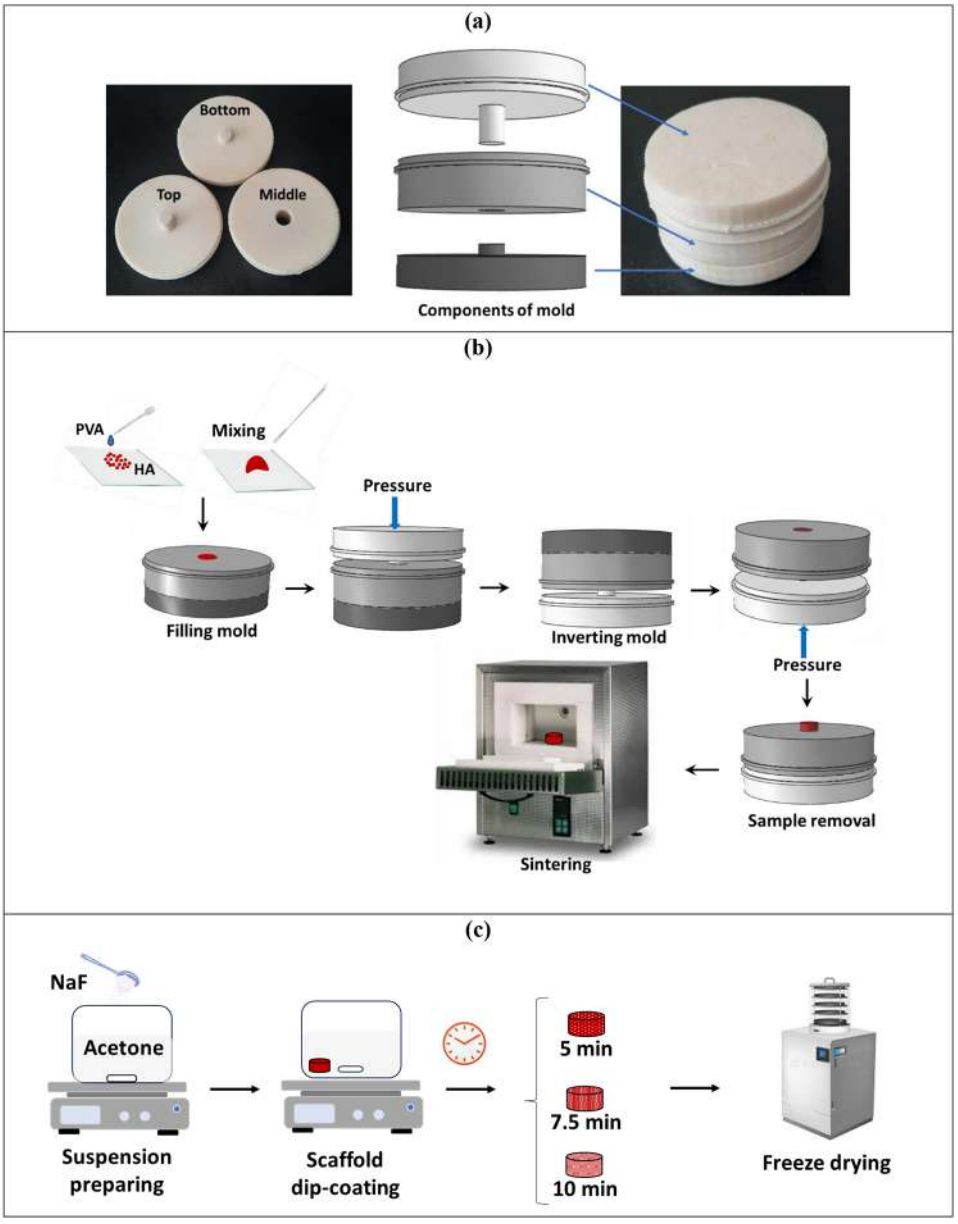

Fig. 1 (**a**) Mold components, (**b**) the procedure used to make n-HA substrates, and (**c**) NaF loading on n-HA substrates

Disc-shaped substrates were divided into three groups for NaF loading based on the immersion time (5, 7.5, and 10 min). The NaF loading process was performed by placing the n-HA substrates in a 75 w/v% suspension of NaF in acetone on a stirrer. To prevent the evaporation of acetone, a lid was placed on the container having the suspension during processing. After the immersion time, the NaF loaded n-HA substrates were frozen at -20℃ and then lyophilized (Freeze-dried) for 24 h (Fig. 1c). The difference between the weights was calculated by weighing the fabricated components before and after NaF loading to estimate the amount of loaded NaF on the n-HA substrates.

Characterizations and porosity of n-HA substrates

The XRD spectrum (Bruker, D8-advance) of the sintered n-HA substrate was conducted in the 2θ range of 10–80°. Furthermore, SEM (Philips XL30, Netherland) and FE-SEM (MIRA3, TESCAN) images were provided after the n-HA substrate sintering process. The pore size was measured using ImageJ software. Moreover, FE-SEM images (FE-SEM, Sigma 300-HV, Zeiss, Germany) were also provided after loading of NaF on the surfaces of n-HA substrates. First, the materials were sputter-coated by a conductive material and then the images were taken at the secondary electron mode. Additionally, elemental map analysis of the NaF-loaded n-HA substrates was accomplished using energy-dispersive X-ray spectroscopy (EDS). Furthermore, the fabricated components before and after NaF deposition were investigated by Fourier transform infrared spectroscopy (FTIR). The transmission spectra were obtained at wavenumbers of 4000–400 cm^{-1} at the resolution of 2 cm^{-1} using (Bruker-Tensor 27 IR, USA).

To determine the amount of porosity, the volume and mass of each sample were measured to first calculate the density using Eq. 1 and then the porosity by Eq. 2 [34–37].

$$D = \frac{m}{V} \tag{1}$$

$$P\% = 100 \times \left(1 - \frac{D}{D_{th}}\right) \tag{2}$$

Where, D, m and V signify the density (kg/m^3), the mass (kg), and the volume (m^3) of each n-HA substrate, respectively. Furthermore, P is the porosity, and D_{th} identifies the theoretical density of hydroxyapatite, which was considered to be 3200 Kg/m^3.

Furthermore, the porosity was also measured by liquid displacement method, in which ethanol was used as the displacement liquid because it could readily infiltrate into the n-HA substrate pores without inducing swelling or shrinkage, and substrate dissolution. First, the substrates were immersed in ethanol with a certain initial volume (v_1). After 5 min, the total volume (ethanol+substrate) was recorded (v_2). The n-HA substrates were then taken out from the ethanol and the remaining ethanol volume was measured (v_3). Finally, the porosity was calculated by Eq. 3 [38].

$$P\% = 100 \times \left(\frac{v_1 - v_3}{v_2 - v_3}\right) \tag{3}$$

NaF release profile and pH changes

For evaluation of the loading efficiency and NaF release, the disc-shaped n-HA substrates loaded with NaF were individually put in containers filled with 15 mL of phosphate-buffered saline (PBS). At different time points, until 14 days, 200 µL of the PBS was taken from each container to measure the optical density (absorbance) at 630 nm using a microplate reader (Synergy H1 Hybrid Multi-Mode Microplate Reader, BioTek, USA). After each sampling, an amount equal to the removed sample was replaced with PBS. A standard curve of NaF concentration-optical density was obtained by measuring the absorbance of known NaF concentrations. This standard curve was used to convert the sample absorbance to concentration. The cumulative release (%) of NaF was then calculated and plotted as a function of time. Furthermore, throughout the soaking time, the pH changes of the solutions were recorded using a pH meter (Shimifan. CO, Iran).

Sterilization and preparation of extract medium

For sterilization, the fabricated components were covered individually with aluminum foil and placed in glass sterile Petri dishes, which were kept in an oven at 170 °C for 30 min. They were then transferred under a laminar cell culture hood. To prepare the extract medium, after sterilization, two samples from each group were immersed in a complete culture medium (2.0 ml/well) in a 24-well plate for 3 days. Afterward, the samples were discarded and the culture media were used for the cellular tests (based on ISO 10993-5-1999).

Cell culture

Dental pulp stem cells (DPSCs) were purchased from Royan Stem Cell Technology (Isfahan, Iran). Dulbecco's Modified Eagle Medium (DMEM, Gibco, Grand Island, USA) that contained 10% fetal bovine serum (FBS, Gibco, Grand Island, USA), Penicillin (100IU), Streptomycin (100 µg/mL) were used as a cell culture medium. The cells were grown in the presence of 5% CO_2 and 95% humidity at 37 °C.

Cytotoxicity tests

The viability of the cells exposed to the extract medium was evaluated by a lactate dehydrogenase (LDH) cytotoxicity detection kit (Roche Applied Science, Germany). DPSCs cells (5×10^3 cells per well) were seeded in a 96-well plate in a complete growth medium (DMEM/F12+10% FBS) for 24 h to form a monolayer. The medium was then replaced by the extract media. After 3 and 7 days of incubation, the plate was centrifuged, and the supernatants were transferred to another 96-well ELISA plate. After that, the LDH detection mixture was inserted into the plate wells (100 µL per well), which were then incubated at room temperature (30 min). The optical density was measured by a microplate ELISA reader at 490 nm (Synergy H1 Hybrid Multi-Mode Microplate Reader, BioTek, USA). The cell viability was calculated by Eqs. 4 and 5.

$$\text{Cytotoxicity } (\%) = \frac{\text{experimental value } - \text{ low control}}{\text{high control } - \text{ low control}} \times 100 \quad (4)$$

$$Viability\,(\%) = 100 - Cytotoxicity \quad (5)$$

Where the low control was a mixture of the supernatants of cells cultured without extract medium and the LDH detection mixture. Furthermore, the high control was prepared by lysing the cells with triton X-100.

Alkaline phosphatase assay

DPSCs at a density of 2×10^3 cells per well in a 96-well plate were cultured in a complete culture medium for 24 h to form a cell monolayer. The medium was then replaced by extract media, and osteogenic factors including ascorbic acid (vitamin C, 50 µg/mL), and β-glycerophosphate (10mM) (Sigma-Aldrich, USA) were also added. ALP activity was measured using the SensoLyte pNPP Alkaline Phosphatase Assay Kit (AnaSpec, USA) according to the protocol provided by the manufacturer. Briefly, 7 and 14 days after cell culture with extract media, cells were homogenized in 100 µL lysis buffer provided with the kit. The obtained lysate was centrifuged for 15 min at 10,000 g, 4° C. The supernatant was collected for ALP assay using p-nitrophenyl phosphate (p-NPP) as a phosphatase substrate (for 20 min at room temperature). The alkaline phosphatase standard was supplied with the kit. The absorbance was measured at 405 nm (Synergy H1 Hybrid Multi-Mode Microplate Reader, BioTek, USA).

Table 1 The sequence of primers used in RT- PCR

Sequence	Name
B2m	F: 5′-CGTGATCTTTCTGGTGCTTGTC-3′ R: 5′-GGAAGTTGGGCTTCCCATTCT-3′
Col1a1	F: 5′-AAGAGCGGAGAGTACTGGAT-3′ R: 5′-CTTGGGGTTTGGGCTGATGT-3′
RUNX2	F:5′-GGAACCAAGAAGGCACAGAC-3′ R: 5′-CGGGACACCTACTCTCATACT-3′
VEGF-A	F: 5′- TCGGAGAGCAACGTCACTA-3′ R: 5′- TCTTTGGTCTGCATTCACATC-3′

Osteocalcin assay

DPSCs cells (5×10^3 cells per well) were seeded in a 96-well plate and cultured in a complete growth medium for 24 h allowing cells to form a monolayer. The complete medium was then replaced by extract media. After 7 days of incubation, the osteocalcin level was assessed in the cell culture supernatant by a sandwich ELISA method using rat osteocalcin/bone gamma-carboxyglutamic acid-containing protein (OT/BGLAP) ELISA Kit (Zell-Bio, Germany) according to the instruction provided by the manufacturer.

Gene expression analysis by RT-PCR (qRT-PCR)

The RT-PCR analysis was conducted based on previous studies [39–41]. Assessment of bone-specific and angiogenic genes in the DPSCs cultured in the extract media after 3 days including Runx2, type I collagen (COLI), and vascular endothelial growth factor (VEGF) involved in bone differentiation was performed using real-time polymerase chain reaction (RT-PCR).

Total RNA from cells was isolated using TRIzol reagent (Invitrogen). The cDNA was synthesized according to the protocol of the Revert Aid™ First Strand cDNA Synthesis Kit (Takara, Japan). The cDNA was synthesized and the expression levels of Runx2, COLI, and VEGF mRNA were measured and quantified using the Corbett Life Science RT Detection System and the SYBR Green Master Mix Kit (Takara). B2M was the endogenous control used to normalize the mRNA expression levels. The primer sequences are shown in Table 1. This real-time quantitative PCR (RT-qPCR) approach allows precise measurement of gene expression, with B2M serving as a reliable internal reference for analysis. Our data were analyzed using the 2-ΔΔC method.

Cell adhesion test

For cell adhesion, DPSCs (2×10^3 cells per well) were directly seeded onto the surfaces of n-HA substrates with and without NaF and incubated at 37 °C, 5% CO_2, and 95% humidity. After 3 days of incubation, the cells on the samples were fixed with paraformaldehyde (4%) at 4℃ for 20 min, rinsed with PBS, dried, and gold-coated to observe under SEM (FE-SEM, Sigma 300-HV, Zeiss, Germany).

Statistical analysis

All data were analyzed using the analysis of variance (ANOVA) test using Minitab V17. The P-values <0.05 (confidence level 95%) were considered significant.

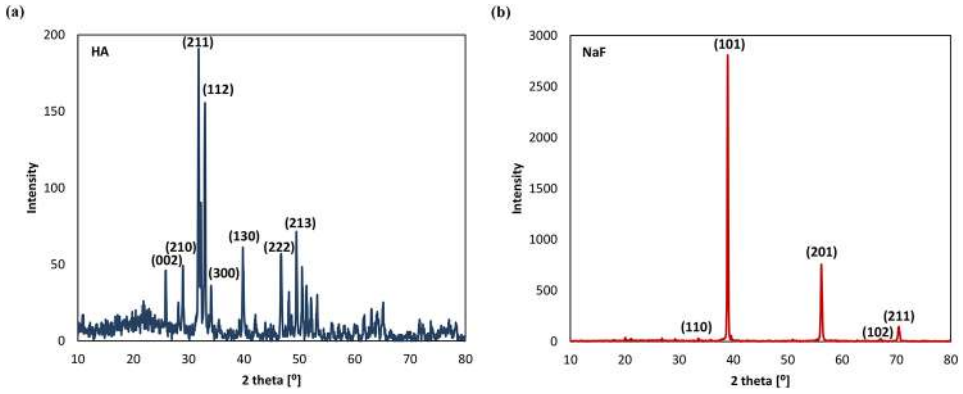

Fig. 2 XRD patterns of; (**a**) HA, and (**b**) NaF powders

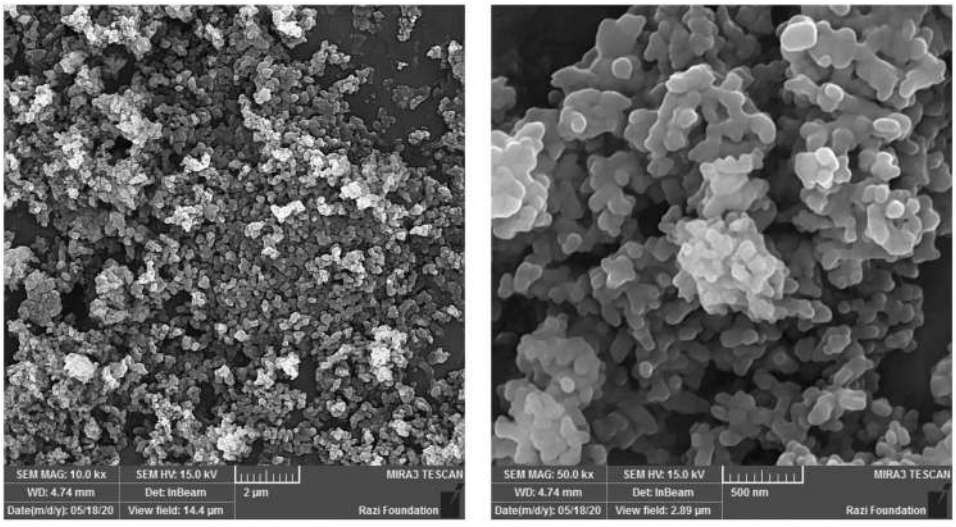

Fig. 3 FE-SEM images of HA powder after 2 h of ball mill, with different magnifications

Post-hoc analysis was performed via Tukey's multiple comparison test.

Results

Characteristics of HA and NaF powder

Figures 2a and 3 show the XRD pattern and SEM images of HA powder, respectively. The obtained XRD spectrum matched the hydroxyapatite reference card of 24–0033, and that reported in previous studies [42–44]. The HA main peaks appeared at 2θ around 31.8°, 32.2°, and 32.9°, which are associated with diffraction planes of (211), (112), and (300), respectively (Fig. 2a). Furthermore, the SEM images (Fig. 3) showed that HA powder size became at nano-scale level after 2 h of ball mill.

The XRD pattern of NaF powder is shown in Fig. 2b. The obtained XRD pattern matched the NaF reference card of 36-1455 and that of previously reported data [45, 46]. The results indicated a very well-crystallized structure of NaF with diffraction at 2θ of about 33.65°, 38.95°, 56.20°, 67.07°, and 70.41°, respectively, from Miller indices of (110), (101), (201), (102) and (211).

n-HA substrate morphology, phases, and porosity

Figure 4a shows the SEM images of a nano-hydroxyapatite substrate after 1 h sintering at 1100℃. As it can be seen, the fabricated substrates were porous with rough surfaces after sintering, which can cause superior performance in a biological environment and new bone growth in vivo [47, 48]. The pore size distribution was mainly in the range of 125–2375 nm and the mean pore size was 1083 nm (Fig. 4b). Furthermore, the XRD peaks (Fig. 4c) that appeared for n-HA substrates sintered at 1100 °C in the electric furnace represented the same characteristic peaks as those of HA powder (raw material) and are in agreement with previous studies [49–54]. Therefore, no phase changes happened after sintering at 1100℃.

Figure 5 represents the FF-SEM images of nano-hydroxyapatite substrates after immersion in NaF suspension for 5 min, 7.5 min, and 10 min. As it can be observed, small particles were settled down on the surfaces of scaffolds, which were believed to be NaF. By increasing the time from 5 to 10 min, the amount of these small particles increased on the substrate surfaces.

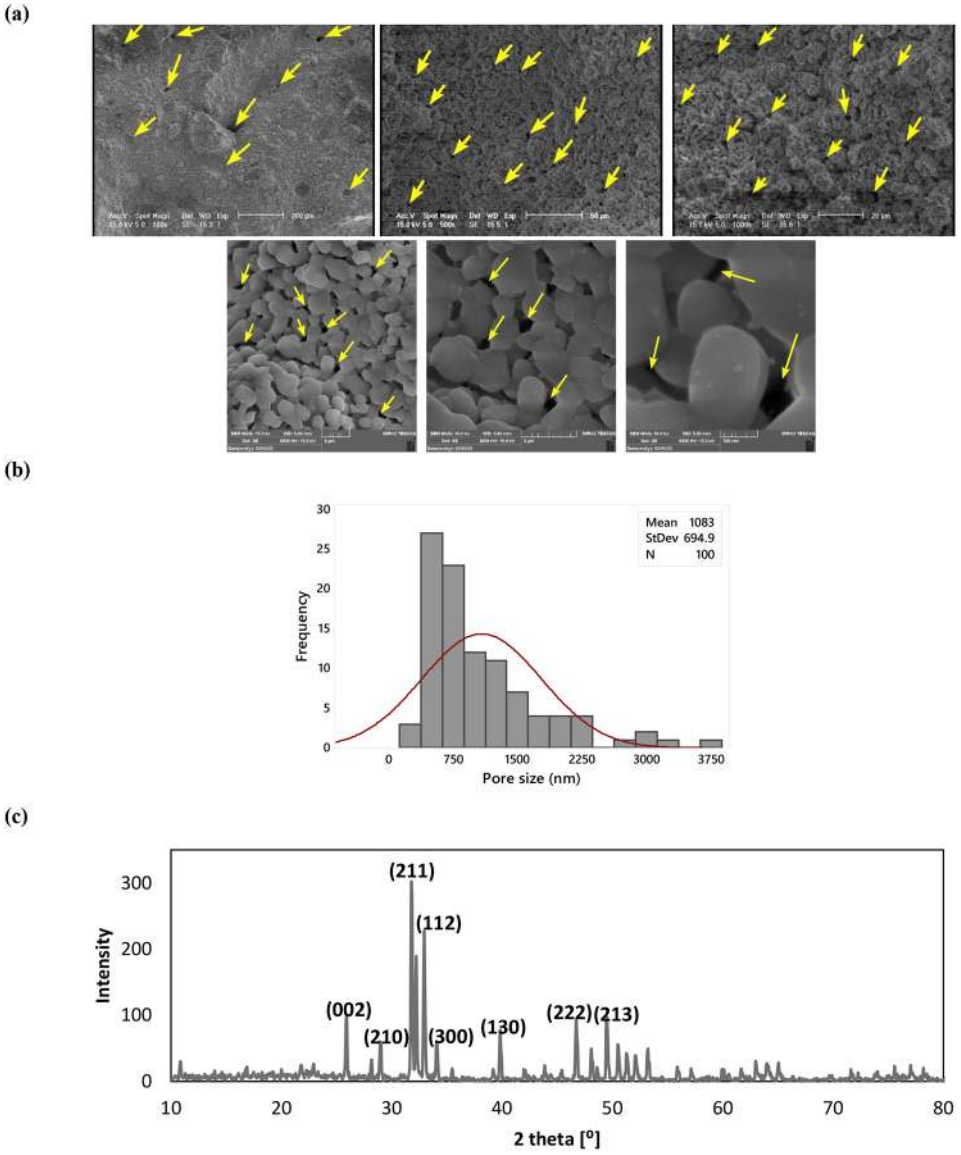

Fig. 4 (**a**) SEM and FE-SEM images of the n-HA substrates after sintering and before immersion in NaF suspension (The arrows show some of the pores.), (**b**) pore size distribution, and (**c**) XRD pattern of the fabricated n-HA substrates

Furthermore, the map analysis (Fig. 6) indicated the deposition of similar elements on the surfaces of all n-HA substrates. The presence of Ca and P are indicative of substrate composition (hydroxyapatite), and the existence of Na and F identifies the deposition of these elements on the surfaces of n-HA substrates after immersion in NaF suspension.

The n-HA substrates before and after NaF deposition were also investigated by FTIR (Fig. 7). It can be clearly realized that all the n-HA substrates with and without NaF have a highly similar absorption spectrum. The only effect of NaF on the FTIR spectrum of n-HA substrates was the slight shifts and the changes in intensity of some of the detected peaks (Table 2). Similarly, previous studies have reported that the addition of NaF to other materials often causes a shift in the FTIR peaks with no additional bonds [55–57]. In the n-HA FTIR pattern, the bands in 632.61 cm^{-1} and 3571.92 cm^{-1} identify hydroxyl groups [58, 59]. The phosphate peaks were detected in the range of 1100 – 1000, and at 962, and 603 cm^{-1} [60]. The blunt bond, usually observed around 3400 cm^{-1}, is water molecules [61], and the weak characteristics peaks at a range of 1400–1500 cm^{-1} are related to carbonate bands [42, 43, 62, 63]. The band that appeared at about 1640 cm^{-1} is associated with hydrogen phosphate (HPO_4^{2}), and those in the range of 3000 – 2800 cm^{-1} identify Alkane [58, 64–66].

The density and porosity of the n-HA substrates were also obtained. Based on the weighting approach, the density and porosity were 1658.56±316.00 kg/m^3, and

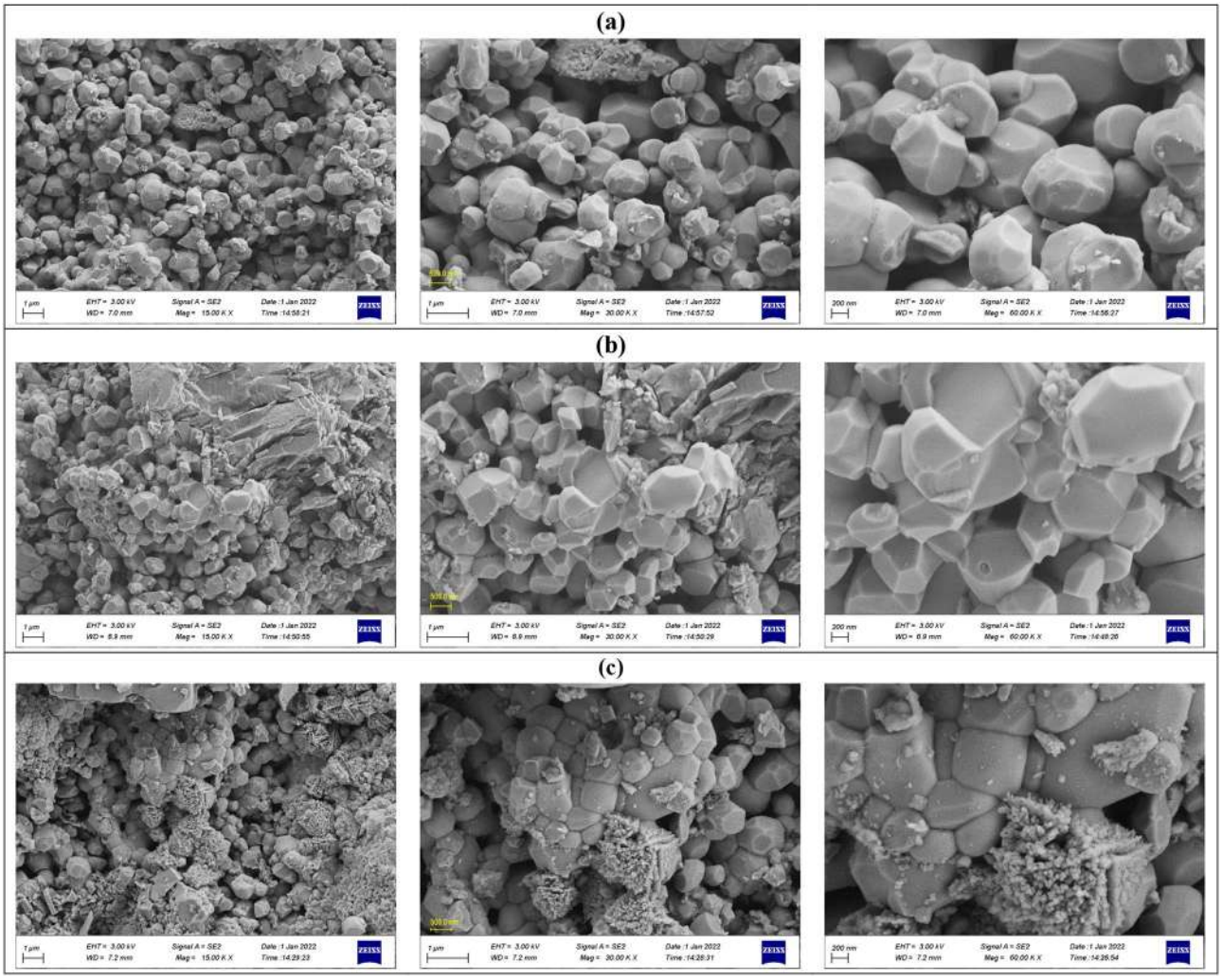

Fig. 5 FE-SEM images of the n-HA substrates after (**a**) 5 min, (**b**) 7.5 min, and (**c**) 10 min immersion in NaF suspension

48.87±9.37%, respectively. According to liquid displacement method, the porosity was 42.73±2.73%.

NaF deposition and release, and solution pH

The deposited amount of NaF on the surfaces of n-HA substrates is shown in Fig. 8a and b. As it was expected, more NaF was deposited by increase in immersion time; 6.43 mg (64.30 mg/mm^2), 4.50 mg (43.26 mg/mm^2), and 1.47 mg (13.42 mg/mm^2), respectively for 10 min, 7.5 min, and 5 min of immersion in NaF suspension. The results of NaF release (Fig. 9a) indicated a relatively higher release of NaF for an immersion time of 5 min. While the lowest release was from the samples with 7.5 min immersion. The NaF release was 39.06%, 36.43%, and 39.57% for 10, 7.5, and 5 min, respectively, after 1 day of immersion. Nevertheless, the release rate became relatively slow after day 1. The NaF release rates were 60.95%, 55.38%, and 69.72% for 10, 7.5, and 5 min, respectively, at day 14 (Fig. 9a).

The pH of the immersion medium was recorded at different time intervals for 14 days (Fig. 9b). The pH of the medium related to all n-HA substrates with and without NaF was mainly changed during the first 4 days of immersion. At day 4, the pH of the media increased from 7.38 to a pH of about 7.85, 7.84, 7.63, and 7.66 for C0, C5, C7.5, and C10, respectively. Moreover, it was observed that the substrates with higher time for NaF settlement (C7.5 and C10) showed lower pH increases. The pH of media associated with the C7.5, and C10 increased up to 4 days and remained relatively constant until day 14, probably as a result of equilibrium in ion exchange in the solution.

Cytotoxic effect

The release of LDH is a marker for cell death. We, therefore, assessed whether the treatment of cells with the substrates having different doses of NaF (C5, C7.5, and C10) resulted in the LDH release. As shown in Fig. 10a, the

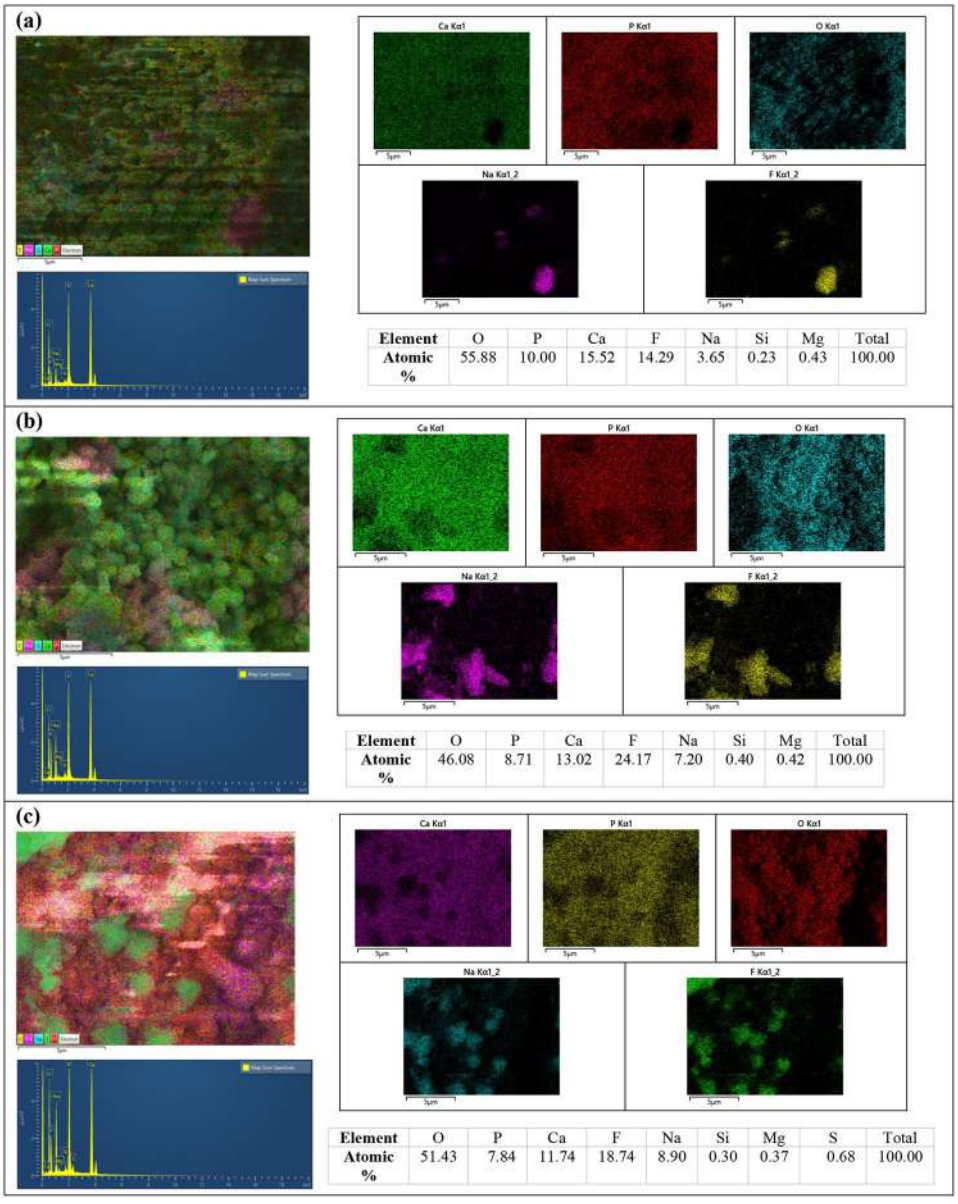

Fig. 6 EDS results of the n-HA substrates after (**a**) 5 min, (**b**) 7.5 min, and (**c**) 10 min immersion in NaF suspension

results revealed that all fabricated components showed no cytotoxic effects on DPSCs (viability% > 100%). One-way ANOVA indicated that the sample composition was not a significant factor ($P=0.075$) meaning that the amount of NaF on the substrates did not influence the cell viability. Furthermore, Tukey pairwise comparisons showed that the cell viability was not significantly different between the groups (Fig. 10a).

ALP activity

ALP analysis was conducted to assess the differentiation of DPSCs to osteoblasts exposed to the extract medium at two time intervals. Cell differentiation was assessed in terms of the ALP activity of the DPSCs after culturing with extract media for 7 and 14 days (Fig. 10b). The DPSCs differentiation (ALP concentration) of all groups was similar, and the ALP activity slightly decreased by the culture time from day 7 to day 14 (Fig. 10b). Two-way ANOVA was employed for analysis and revealed that sample composition and time were significant factors ($P = 0.002$, and $P=0.000$, respectively) in ALP activity. The Tukey pairwise comparisons also showed significant differences between the substrate without NaF (C0) and those with 5 min and 10 min immersion in NaF suspension (C5, and C10) at day 7. However, there was no statistical difference between the groups at day 14.

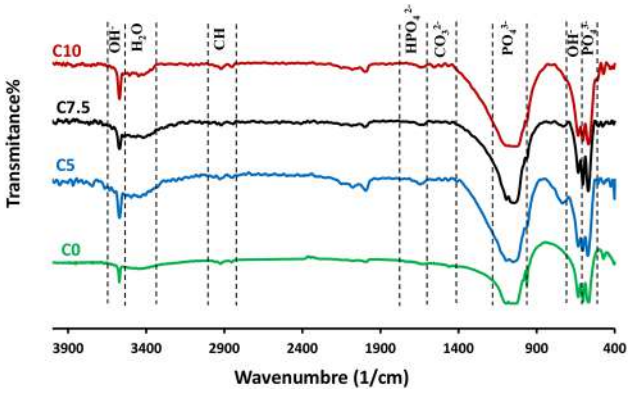

Fig. 7 FTIR spectra before (C0) and after NaF deposition (C5, C7.5, and C10)

Osteocalcin concentration

The osteocalcin levels (OSC) in the DPSCs culture medium, shown in Fig. 10c, were lower in the groups with different doses of NaF rather than in the substrate without NaF (C0), and even the control group (C, cells without treatment). One-way ANOVA showed that the sample composition was not a significant factor (P=0.092) meaning that the amount of NaF on the substrate did not influence the osteocalcin concentration. Tukey pairwise comparisons also showed that the osteocalcin level was not significantly different between the groups.

Adhesion of cells to the n-HA substrates

The capability of the substrates on the attachment of DPSCs after 3 days of culture was analyzed by SEM images (Fig. 11). As it can be seen, the adhered cell morphology on different materials (n-HA substrates with and without NaF) was quite similar. The DPSCs were stretched and enlarged multifacetedly on their surfaces.

Gene expression

The RT-PCR was employed to assess the expression level of osteogenic and angiogenic genes including Runx2, COL I, and VEGF of all groups after 3 days (Fig. 12). The C10 and C5 groups displayed higher Runx2, and COL I gene expression, which are associated with early differentiation toward bone cells, than other groups. Regarding the VEGF expression, C10 showed the highest value. One-way ANOVA also showed that the sample composition was a significant factor in Runx2 (P=0.000), COL I (P=0.000), and VEGF (P=0.001). Tukey pairwise comparisons also showed that the Runx2 level was significantly higher in C10 and C5 than in other groups, and in C7.5 compared to C0 and C groups. This analysis for COL I revealed that the gene level was significantly higher in C5 than in all other groups, and in C10 compared to C7.5, C0, and C groups. Moreover, the expression of VEGF was significantly higher in C10 rather than in all other groups.

Table 2 Absorbance bonds observed for different n-HA substrates with and without NaF

	Wavenumber						
C10	3571.92	1091.63	1024.13	964.34	634.54	603.68	568.96
C7.5	3569.99	1093.56	1043.42	964.34	632.61	603.68	568.96
C5	3571.92	1095.49	1051.13	970.13	632.61	605.61	572.82
C0	3571.92	1095.49	1039.56	962.41	632.61	603.68	568.96

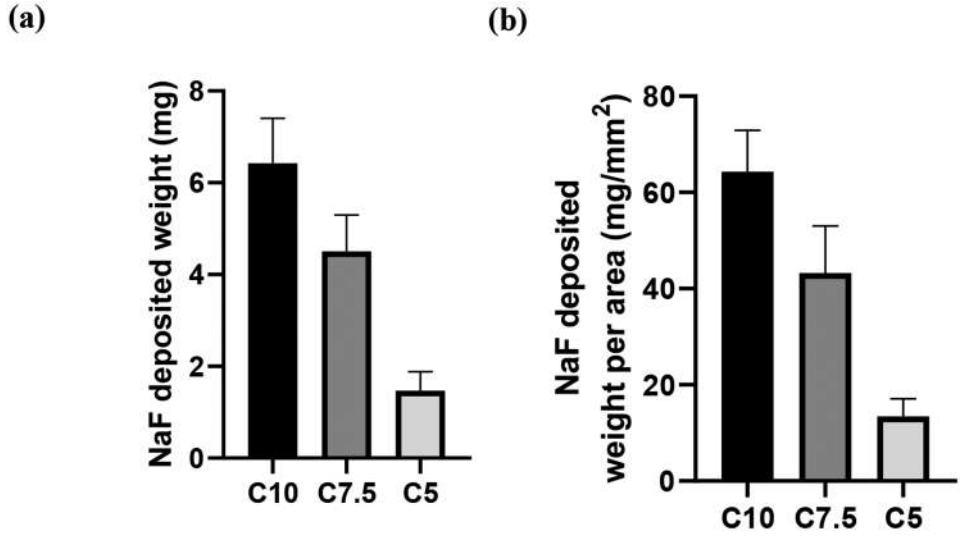

Fig. 8 NaF deposition; (**a**) weight, and (**b**) weight/area

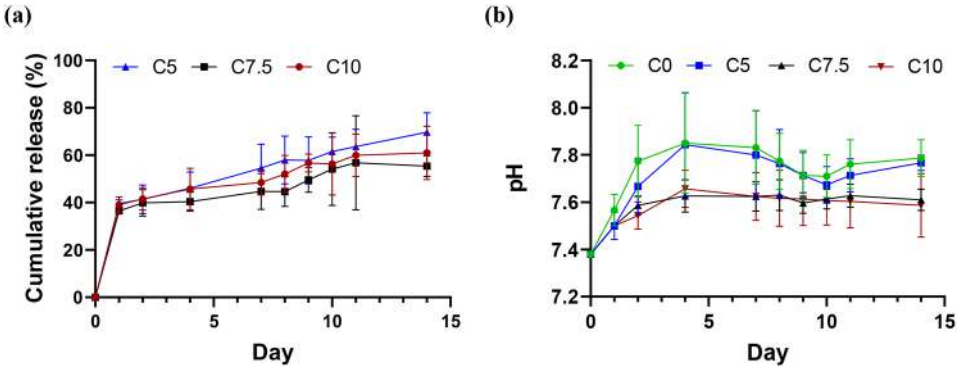

Fig. 9 (**a**) NaF release profile, and (**b**) pH changes of PBS solution

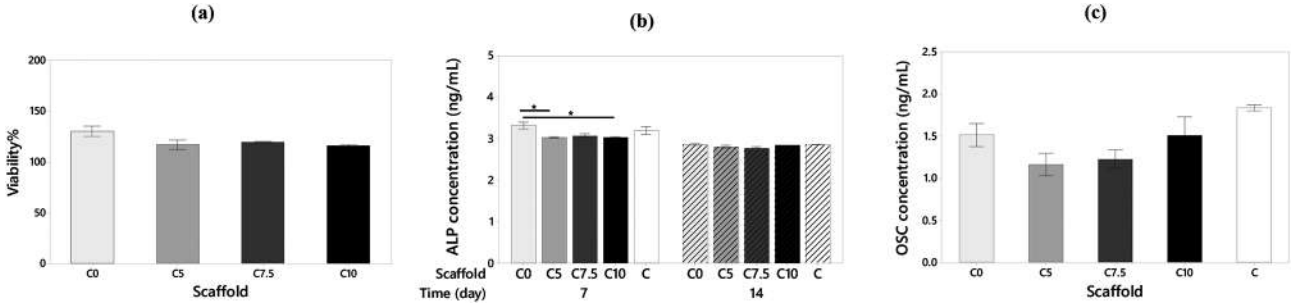

Fig. 10 (**a**) Viability of the cells by LDH assay after 72 h, (**b**) ALP concentration as an indicator for cell differentiation after 7 and 14 days, and (**c**) OSC concentration in different groups after 7 days. (*: $P < 0.05$)

Discussion

Tissue engineering uses biomaterials, stem cells, and biologically active factors such as morphogens to offer a new way for the regeneration of bone and other mineralized tissues such as dentin [67, 68]. Biomaterials are used to fabricate scaffolds, which are often three-dimensional constructs with interconnected pores that facilitate nutrient and waste transport, cell migration, and vascularization [69]. These constructs can be used alone or together with cells and biologically active factors to achieve favorable reparative performance. The scaffolds and other substitutes can be made up of different biomaterials depending on the tissue to be repaired. For hard tissue repair, calcium phosphates are a demanding group because their chemistry is similar to that of hard tissue [70]. Among these materials, HA is a popular biomaterial as it has excellent bioactivity, biocompatibility, adequate mechanical properties, osteoconductivity, angiogenic properties, and without any inflammatory reactions or antigenicity [20]. Nano-sized HA resembles the inorganic part of the extracellular matrix (ECM) of bone, which contains nano-sized calcium phosphate crystallites that are similar to HA [71], and it has been broadly used in dentistry in periodontology, and oral and maxillofacial surgery [72, 73]. NaF is also believed to have an ossifying effect. For these reasons, the biological n-HA from carp bone waste was used here to fabricate porous substrates. The fabricated substrates had porosity with rough surfaces (based on SEM images). The porosity was mainly created by the partial sintering of the hydroxyapatite particles. In partial sintering, high porosity, pore interconnectivity, and increased pore size can be achieved by reducing the applied pressure and/or temperature during consolidation [74, 75]. However, the pore shape tends to be more irregular rather than to be rounded, as it was observed in our SEM images. The porosity of the n-HA substrates was >40%, and the pore size distribution was mainly in the range of 125–2375 nm. It has been reported that a pore diameter of 100 μm and larger is more desirable for better cell attachment and vascularization [76]. The pore characteristics can be influenced by the fabrication process. Therefore, to achieve a larger pore size, other techniques can be used, such as 3D printing with precise control over the internal pore geometry or particulate leaching and the use of space-holder materials [77–83]. For example, Yahay et al. [80] fabricated TiO_2/PCL composite scaffolds using a combination of different techniques including sol-gel, porogen (NaCl) leaching, and direct ink writing. The scaffolds had multiscale porosity (meso and macro pores) with different pore sizes. The porosity percentages and the compressive moduli were respectively in the range of 74.56-80.02% and 4.96–20.03 MPa based on the porogen content.

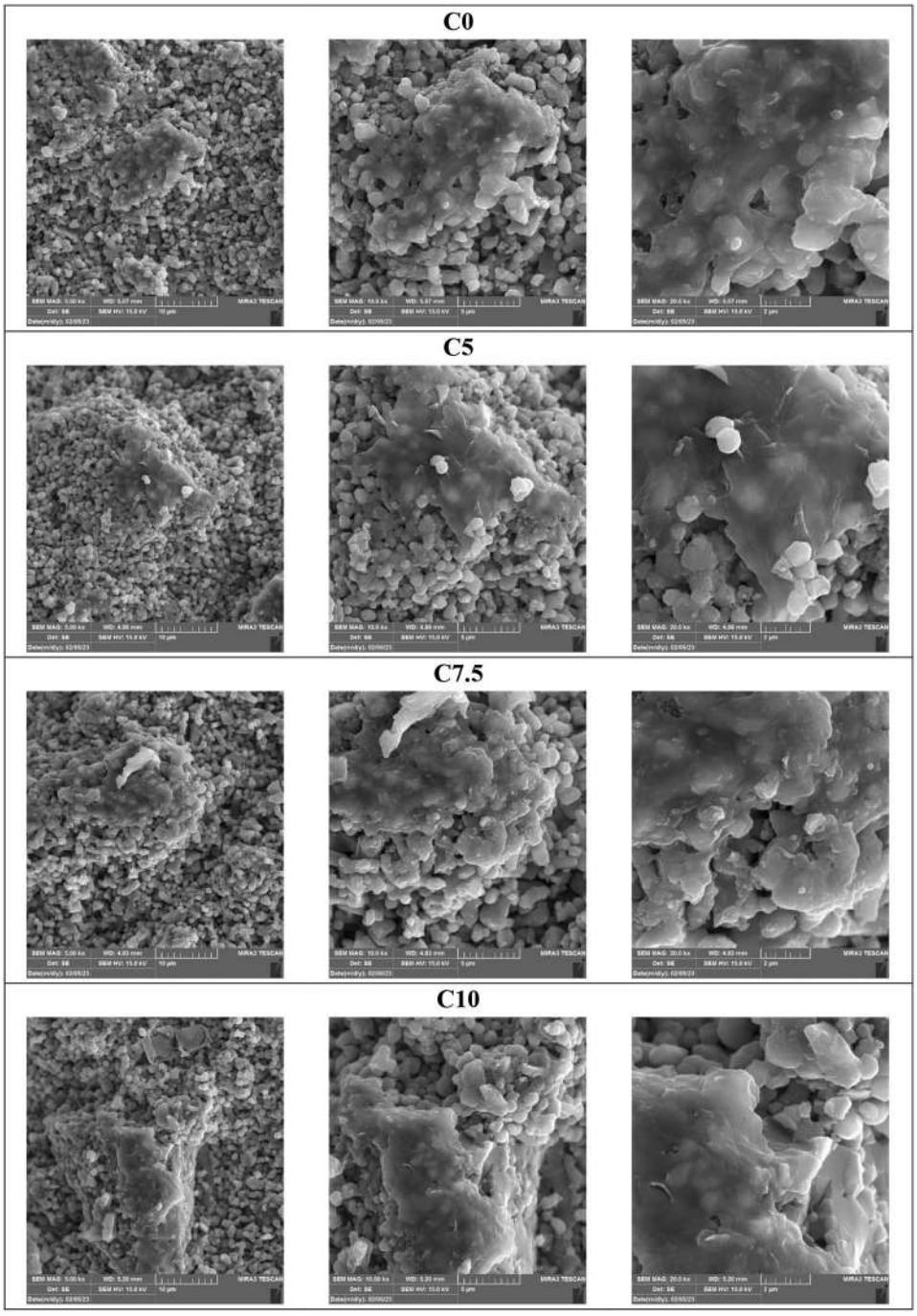

Fig. 11 FE-SEM images of the adhered cells on C0, C5, C7.5, and C10

The porous n-HA substrates were subsequently impregnated with NaF by immersing them in NaF suspension for different times (5, 7.5, and 10 min). To make the NaF suspension, acetone was used. NaF does not dissolve into acetone, and a suspension is provided. While, it is ionized to Na^+ and F^- in aqueous solutions. Here, it was intended to have NaF particles on the substrates which could be ionized later in the culture medium. Considering the in vivo study as a future work, the ionization can occur after implantation and in contact with body fluid. The NaF was successfully settled on the substrates based on SEM, EDS, and FTIR analyses. The type of adsorption of drugs or bioactive molecules to the substrates can be physisorption (physically) or chemisorption (chemically) [84]. The NaF attached physically to the substrate-free surfaces through their soaking in NaF suspension. In this type of adsorption, the molecules bond to a surface with a rather weaker interaction in

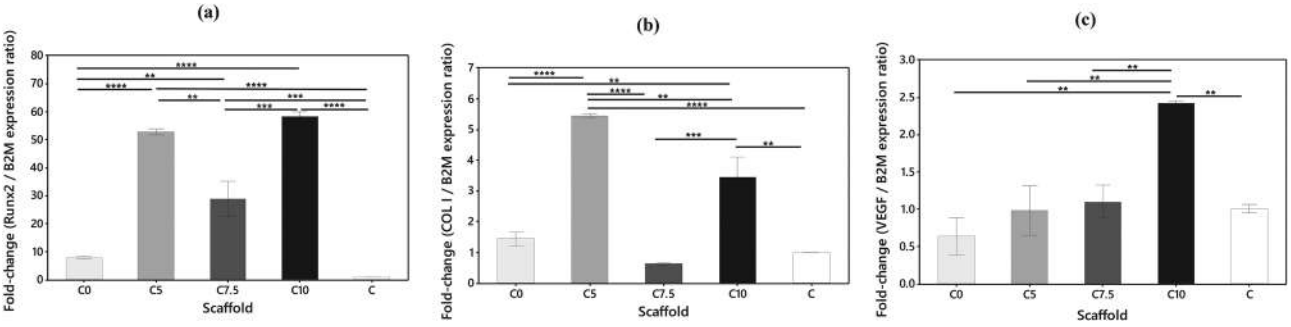

Fig. 12 Evaluation of the relative expression of bone-specific and angiogenic genes in the different groups; (**a**) Runx2, (**b**) COL I, and (**c**) VEGF (*: $P < 0.05$, **: $P < 0.01$, ***: $P < 0.001$, and ****: $P < 0.0001$)

comparison with chemisorption. Physisorption is reversible, therefore, after NaF deposition and drying, when the components were immersed in PBS, the NaF particles started deboning from their surfaces. Nevertheless, its release rate is relatively lower than the loading. This can be due to the presence of porosity in the structure and the trap of the NaF within the pores, which results in mechanical locking leading to a delay in NaF release [85]. The detachment of NaF from C5 (immersion time of 5 min) was faster than the other groups. It is believed that in this group, the NaF could not penetrate into the substrate pores deep inside the structure due to the limited soaking time in the suspension. Therefore, their NaF content could be readily release. Furthermore, a moderate pH rise of the immersion media was observed, which can be due to a weak basic nature of NaF (a basic salt resulting from a strong base (NaOH) and a weak acid (HF)). Indeed, the anion F^-, is the anion of weak acid HF, hence, F^- acts as a base. In the present study, it was observed that the substrates with higher time for NaF settlement (C7.5 and C10) showed lower pH increases; possibly due to the slightly lower amount of the F^- ions released into the solution from these substrates.

Furthermore, in the present study, gene analysis was also conducted. During the osteogenic differentiation process, the expression level of several genes such as Runx2, COL I, DSPP, BMP2, ALP, Osterix, Osteopontin (OPN), sialoprotein (BSP), and OSC are elevated indicating the stem cells are differentiated toward osseous tissue. Some of these genes contribute to early osteogenic differentiation such as BMP-2, Runx2, Osterix, ALP, and COL I, while others including OSC, OPN, and BSP involve in late osteogenic differentiation [86, 87]. It has been identified that the first markers for differentiation are ALP and COL I, and subsequently, BSP is detected (2–3 days later), followed by the expression of OSC and nodule mineralization [88]. In the present study, we measured Runx2, COL I, and VEGF. Runx2 is a specific transcription factor for osteoblast differentiation, matrix formation, and mineralization during bone formation, which controls the expression of genes related to the main bone matrix proteins via a direct binding location existing in the promoter of some osteoblast-specific genes including OSC, OPN, BSP, and collagen type I alpha 1 (Col1A1) [89]. COL I is well-known as the most abundant component of ECM and found in tendons, the endomysium of myofibrils, scar tissue, and the organic portion of bone, which plays a role in osteogenic differentiation [90]. COL I can bind to the members of the transforming growth factor (TGF) superfamily including TGF-β and BMPs (bone-inducing growth factors), and is effectual in the healing of bone through inflammatory cytokines and BMP gene expression in the early fracture healing stages [91]. VEGF is another important gene in the bone repair process. The differentiation and function of osteoblasts and osteoclasts are directly controlled by VEGF, and it, indeed, contributes to osteogenesis by stimulating angiogenesis [92]. Nevertheless, it would be interesting to consider the expression of other genes in future research, particularly those involved in late osteogenic differentiation.

The NaF was previously incorporated into the HA-Al_2O_3 nano-composite and chitosan/HA-Al_2O_3 scaffolds for application in bone tissue engineering. The phases of the samples, microstructure, morphology, mechanical strength, and cytotoxicity were studied and it was shown that the addition of NaF into the scaffolds increased the mechanical strength and caused acceptable cell viability [93]. Zijah et al. [94] also evaluated and compared the effect of NaF, melanocyte-stimulating hormone (MSH), or simvastatin (SIM) on nanofibrous PCL-polyethylene glycol-PCL (PCL-PEG-PCL) scaffold on human DPSCs (hDPSCs). Nanofibrous scaffold-seeded with hDPSCs were treated with these materials and the cell viability, biocompatibility, cell attachment, proliferation, morphology, osteo/odontogenic potential, and the tissue-specific gene expression were analyzed. Their results showed that all the treated scaffolds performed superiorly compared to the control untreated group. However, SIM and MSH showed significantly better results than NaF. In another study, by Aghazadeh et al. [9], NaF was added to the cell culture medium and investigated for its synergistic effect with the electrospun poly(ε-caprolactone)

(PCL)/polylactic acid (PLA) nanofiber scaffolds with and without HA. The authors evaluated the proliferation, osteoblast differentiation, and mineralization of DPSCs exposed to these scaffolds and enriched medium with NaF. They found excellent cell adhesion, proliferation, and mineralization as well as superior osteogenesis markers (Runx2, DSPP, OSC, and BMP2) in the groups with HA and with HA/NaF (in the culture media), where the latter exhibited synergistic effects on the growth and differentiation of DPSCs. Moreover, the effects of micromolar levels of NaF were evaluated on the proliferation and osteogenic differentiation of preosteoblasts MC3T3-E1 cell line without using scaffolds [29]. The results of this study showed that NaF could significantly enhance the proliferation, ALP activity, and mineralization of the cells, and up-regulate the expression of mRNAs encoding Runx2, Osterix, Osteopontin, and Osteocalcin in the NaF-treated group rather than the untreated controls. In the present study, similar results were obtained with regard to viability. We found acceptable cytocompatibility with DPSCs and superb cell attachment in all groups. The elevated Runx2, COL I, and VEGF gene expression was observed in the substrates with 10 min immersion in NaF suspension (C10, 6.43 mg NaF loaded on each substrate). Furthermore, the substrates with 5 min immersion in NaF suspension (C5, 1.47 mg NaF loaded on each substrate) also showed similar results to those of the n-HA substrates with 10 min immersion in NaF suspension, except for VEGF gene expression. However, the COL I level in the C10 was slightly lower than C5, while Runx2 and VEGF levels were higher in the C10 group. The n-HA substrates immersed for 7.5 min in NaF suspension (C7.5, 4.50 mg NaF loaded on each substrate), caused lower expression of Runx2 and COL I than in C5 and C10 groups, and even lower levels of COL I than C0 group (only n-HA substrates without NaF). Nevertheless, in our study, the evaluation of osteogenic differentiation of DPSCs at the protein level showed no positive effects.

Conclusions

In this study, the structural, physical, biocompatibility, and osteogenic properties of porous sodium fluoride-loaded nano-hydroxyapatite substrates were investigated. First, the nano-hydroxyapatite substrates were made by molding and sintering process. Then the substrates were impregnated with sodium fluoride by immersion in a NaF suspension at different times. The porous substrates were successfully fabricated with acceptable porosity % and NaF loading. The NaF was released sustainably and the pH changes occurred mostly during the first 4 days of immersion. The LDH assay showed no cytotoxicity of the fabricated materials. Furthermore, favorable cell adhesion was observed, in which DPSCs were stretched and enlarged multifacetedly on the surfaces. Moreover, increased Runx2, COL I, and VEGF gene expression was observed in the substrates upon immersion in NaF suspension for 10 min (6.43 mg NaF on each substrate). In addition, the substrates with 5 min immersion in NaF suspension (1.47 mg NaF on each substrate) showed similar results to those with 10 min immersion in NaF suspension, except for VEGF gene expression. However, COL I level was slightly lower in the C10 than in the C5, while Runx2 and VEGF levels were higher in the C10 group. Nonetheless, the evaluation of osteogenic differentiation of DPSCs at the protein level did not show any positive effects in our study.

Supplementary Information

The online version contains supplementary material available at https://doi.org/10.1186/s12903-024-04987-z.

Supplementary Material 1

Acknowledgements
The authors would like to thank Semnan University of Medical Sciences for funding this work.

Author contributions
Marjan Bahraminasab: conceptualization, experiment design, experiment, data analysis, provision of study materials and equipment, draft preparation, writing and reviewing. Samaneh Arab: experiment design, analysis, writing and reviewing. Samira Asgharzade: experiment and analysis, Ali Doostmohammadi: experiment and preparing figures, Zahra Khatib Zadeh: experiment and writing, Vajihe Taghdiri Nooshabadi: methodology and writing.

Funding
This study was funded by Semnan University of Medical Sciences (NO: A-10-404-6).

Data availability
The datasets used and/or analyzed during the current study available from the corresponding author on reasonable request.

Declarations

Ethics approval and consent to participate
This article does not contain any studies with human participants or animals performed by any of the authors (IR.SEMUMS.REC.1400.047).

Consent for publication
Not applicable.

Competing interests
The authors declare no competing interests.

Received: 24 March 2024 / Accepted: 1 October 2024
Published online: 14 October 2024

References

1. Chen F, et al. Anchoring dental implant in tissue-engineered bone using composite scaffold: a preliminary study in nude mouse model. J Oral Maxillofac Surg. 2005;63(5):586–91.
2. Al Maruf DA, et al. Hydrogel: a potential material for bone tissue Engineering repairing the Segmental Mandibular defect. Polymers. 2022;14(19):4186.

3. Zhao Q, et al. Human periodontal ligament stem cells transplanted with nanohydroxyapatite/chitosan/gelatin 3D porous scaffolds promote jaw bone regeneration in swine. Stem Cells Dev. 2021;30(10):548–59.
4. Chang PC, et al. Regeneration of critical-sized mandibular defect using a 3D-printed hydroxyapatite-based scaffold: an exploratory study. J Periodontol. 2021;92(3):428–35.
5. Kim I-H, et al. In vivo evaluation of decellularized human tooth scaffold for dental tissue regeneration. Appl Sci. 2021;11(18):8472.
6. Danesi AL, et al. Uniaxial hydroxyapatite growth on a self-assembled protein scaffold. Int J Mol Sci. 2021;22(22):12343.
7. Earthman JC, et al. Tissue engineering in dentistry. Clin Plast Surg. 2003;30(4):621–39.
8. Bahraminasab M, et al. Bone scaffolds: an Incorporation of Biomaterials, cells, and Biofactors. ACS Biomaterials Sci Eng. 2021;7(12):5397–431.
9. Aghazadeh M, et al. Towards osteogenic bioengineering of dental pulp stem induced by sodium fluoride on hydroxyapatite based biodegradable polymeric scaffold. Fibers Polym. 2017;18(8):1468–77.
10. Liu C, Xia Z, Czernuszka JT. Design and development of three-dimensional scaffolds for tissue engineering. Chem Eng Res Des. 2007;85(7):1051–64.
11. Bahraminasab M, Edwards KL. Computational tailoring of Orthopaedic Biomaterials: Design principles and Aiding Tools, in Biomaterials in Orthopaedics and Bone Regeneration. Springer; 2019. pp. 15–31.
12. Bahraminasab M. Challenges on optimization of 3D-printed bone scaffolds. Biomed Eng Online. 2020;19(1):1–33.
13. Bahraminasab M, Edwards KL. Biocomposites for hard tissue replacement and repair. In: Sidhu BP, Zitoune S, Yazdani R M, editors. Futuristic composites. Materials Horizons: from nature to nanomaterials. Singapore: Springer; 2018. pp. 281–96.
14. Bahraminasab M, Farahmand F. State of the art review on design and manufacture of hybrid biomedical materials: hip and knee prostheses. Proc Institution Mech Eng Part H: J Eng Med. 2017;231(9):1–29.
15. Nair LS, Laurencin CT. Biodegradable polymers as biomaterials. Prog Polym Sci. 2007;32(8–9):762–98.
16. Jazayeri HE, et al. Polymeric scaffolds for dental pulp tissue engineering: a review. Dent Mater. 2020;36(2):e47–58.
17. Farzin A et al. Scaffolds in dental tissue engineering: a review. Archives Neurosci, 2020. 7(1).
18. Bahraminasab M, Doostmohammadi N, Alizadeh A. Low-cost synthesis of nano-hydroxyapatite from carp bone waste: Effect of calcination time and temperature. International Journal of Applied Ceramic Technology; 2020.
19. Enax J, Epple M. Synthetic hydroxyapatite as a biomimetic oral care agent. Oral Health Prev Dent. 2018;16(1):7–19.
20. Granito RN, et al. Hydroxyapatite from fish for bone tissue engineering: a promising approach. Int J Mol Cell Med. 2018;7(2):80.
21. Tschoppe P, et al. Enamel and dentine remineralization by nano-hydroxyapatite toothpastes. J Dent. 2011;39(6):430–7.
22. Bordea IR, et al. Nano-Hydroxyapatite use in dentistry: a systematic review. Drug Metab Rev. 2020;52(2):319–32.
23. Murugan R, Ramakrishna S. Bioresorbable composite bone paste using polysaccharide based nano hydroxyapatite. Biomaterials. 2004;25(17):3829–35.
24. Du M, et al. Recent advances in biomedical engineering of nano-hydroxyapatite including dentistry, cancer treatment and bone repair. Compos Part B: Eng. 2021;215:108790.
25. Munir MU, et al. Nano-Hydroxyapatite as a delivery system: overview and advancements. Artif Cells Nanomed Biotechnol. 2021;49(1):717–27.
26. Bayani M, et al. Main properties of nanocrystalline hydroxyapatite as a bone graft material in treatment of periodontal defects. A review of literature. Biotechnol Biotechnol Equip. 2017;31(2):215–20.
27. Hanafy RA, et al. Biomimetic chitosan against bioinspired nanohydroxyapatite for repairing enamel surfaces. Bioinspired Biomim Nanobiomaterials. 2019;9(2):85–94.
28. Wang X, et al. Biphasic functions of sodium fluoride (NAF) in soft and in hard periodontal tissues. Int J Mol Sci. 2022;23(2):962.
29. Lee M, Arikawa K, Nagahama F. Micromolar levels of sodium fluoride promote osteoblast differentiation through Runx2 signaling. Biol Trace Elem Res. 2017;178(2):283–91.
30. Mendoza-Schulz A, et al. The effects of fluoride on cell migration, cell proliferation, and cell metabolism in GH4C1 pituitary tumour cells. Toxicol Lett. 2009;190(2):179–86.
31. Minim PR, et al. The combined effects of binder addition and different sintering methods on the mechanical properties of bovine hydroxyapatite. J Mech Behav Biomed Mater. 2023;144:105993.
32. Indra A et al. The effect of PVA addition as binders on the properties of hydroxyapatite sintered body. Proceedings of the 2nd International Conference on Industrial and Technology and Information Design, ICITID., 2021, 30 August 2021, Yogyakarta, Indonesia, 2021.
33. Lett JA, et al. The fabrication of porous Hydroxyapatite Scaffold using Gaur Gum as a Natural Binder. Volume 13. Digest Journal of Nanomaterials & Biostructures (DJNB); 2018. 1.
34. Wang J, et al. Biomimetically Ornamented Rapid Prototyping fabrication of an apatite-collagen-polycaprolactone Composite Construct with Nano-Micro-macro Hierarchical structure for large bone defect treatment. ACS Appl Mater Interfaces. 2015;7(47):26244–56.
35. Bahraminasab M, et al. Material tailoring of the femoral component in a total knee replacement to reduce the problem of aseptic loosening. Mater Des (1980–2015). 2013;52:p441–451.
36. Xia Z, et al. Fabrication and characterization of biomimetic collagen-apatite scaffolds with tunable structures for bone tissue engineering. Acta Biomater. 2013;9(7):7308–19.
37. Jahan A, Bahraminasab M. Multicriteria Decision Analysis in improving quality of design in femoral component of knee prostheses: influence of interface geometry and material. Advances in Materials Science and Engineering; 2015.
38. Lee JM, et al. Facile pore structure control of poly (ε-caprolactone) nanofibrous scaffold by salt-dispenser aided electrospinning. J Nanoengineering Nanomanuf. 2013;3(4):269–75.
39. Ponchel F. Real-time PCR using SYBR® Green, in Real-time PCR. Taylor & Francis; 2007. pp. 167–82.
40. Houghton SG, Cockerill FR. Real-time PCR: overview and applications. Surgery. 2006;139(1):1–5.
41. Schmittgen TD, Livak KJ. Analyzing real-time PCR data by the comparative CT method. Nat Protoc. 2008;3(6):1101–8.
42. Sagadevan S, Dakshnamoorthy A. Synthesis and characterization of nano-hydroxyapatite (n-HAP) using the wet chemical technique. Int J Phys Sci. 2013;8(32):1639–45.
43. Abidi SSA, Murtaza Q. Synthesis and characterization of nano-hydroxyapatite powder using wet chemical precipitation reaction. J Mater Sci Technol. 2014;30(4):307–10.
44. Mishra VK, et al. Effect of annealing on nanoparticles of hydroxyapatite synthesized via microwave irradiation: structural and spectroscopic studies. Ceram Int. 2014;40(7):11319–28.
45. Samarehfekri H, et al. Systematic study of naf nanoparticles in micelles loaded on polylactic acid nanoscaffolds: in vitro efficient delivery. J Cluster Sci. 2020;31:453–61.
46. Sarawade PB, et al. Recovery of high surface area mesoporous silica from waste hexafluorosilicic acid (H2SiF6) of fertilizer industry. J Hazard Mater. 2010;173(1–3):576–80.
47. Abbasi N, et al. Porous scaffolds for bone regeneration. J Science: Adv Mater Devices. 2020;5(1):1–9.
48. Shim J-H, et al. Porosity effect of 3D-printed polycaprolactone membranes on calvarial defect model for guided bone regeneration. Biomed Mater. 2017;13(1):015014.
49. Yadav U, Saxena PS, Srivastava A. Simple Route synthesis of hydroxyapatite–gelatin nanocomposite and its characterization. Int J Mater Sci. 2017;12(1):p2017.
50. Mishra VK, et al. Structural and spectroscopic studies of hydroxyapatite nanorods formed via microwave-assisted synthesis route. J Am Ceram Soc. 2012;95(9):2709–15.
51. Kandić L, Mitrić M, Ignjatović N. XRD analysis of calcium phosphate and biocomposite calcium phosphate/bioresorbable polymer. Materials science forum. Trans Tech Publ; 2006;518:507–12.
52. Dudek K, Szaraniec B, Lelatko J, Goryczka T. Structure of multi-layers deposited on NiTi shape memory alloy. Solid state Phenomena. Trans Tech Publ; 2013;203–204:90–3
53. Saeed GK, Essa AF, Said SA-A. Preparation and characterization of hydroxyapatite powder and study of hydroxyapatite-alumina Composite. in Journal of Physics: Conference Series. 2020. IOP Publishing.
54. Venkatesan J, Kim SK. Effect of temperature on isolation and characterization of hydroxyapatite from tuna (Thunnus obesus) bone. Materials. 2010;3(10):4761–72.
55. Thenmozhi M, Suguna K, Sekar C. Influence of sodium fluoride (NaF) on the crystallization and spectral properties of l-tyrosine. Spectrochim Acta Part A Mol Biomol Spectrosc. 2011;84(1):37–42.

56. Xu J, et al. The effects of NaF concentration on electrochemical and corrosion behavior of AZ31B magnesium alloy in a composite electrolyte. RSC Adv. 2017;7(10):5880–7.
57. Lin H et al. Preparation of Drug-loaded Chitosan Microspheres and Its Application in Paper-based PVC Wallpaper. in IOP Conference Series: Materials Science and Engineering. 2018. IOP Publishing.
58. Hammood AS, et al. Effect of calcination temperature on characterization of natural hydroxyapatite prepared from carp fish bones. SN Appl Sci. 2019;1(5):436.
59. Londoño-Restrepo SM, et al. The effect of cyclic heat treatment on the physicochemical properties of bio hydroxyapatite from bovine bone. J Mater Science: Mater Med. 2018;29(5):52.
60. Zhang L, et al. Extraction and characterization of HA/β-TCP biphasic calcium phosphate from marine fish. Mater Lett. 2019;236:680–2.
61. Zhu Q, et al. The preparation and characterization of HA/β-TCP biphasic ceramics from fish bones. Ceram Int. 2017;43(15):12213–20.
62. Chesley M et al. One-step hydrothermal synthesis with in situ milling of biologically relevant hydroxyapatite. Mater Sci Engineering: C, 2020;113:110962.
63. Lü XY et al. Preparation and characterization of natural hydroxyapatite from animal hard tissues. in Key Engineering Materials. Trans Tech Publ; 2007.
64. Geng Z, et al. Synthesis, characterization, and biological evaluation of nanostructured hydroxyapatite with different dimensions. Nanomaterials. 2017;7(2):38.
65. Chen C-H et al. A comparative assessment of implant site viability in humans and rats. J Dent Res 2017;97(4): pp. 451–9.
66. Figueiredo M, Gamelas J, Martins A. Characterization of bone and bone-based graft materials using FTIR spectroscopy. Infrared spectroscopy-life and biomedical sciences, 2012: pp. 315–338.
67. Bahraminasab M, et al. The healing of bone defects by cell-free and stem cell-seeded 3D-printed PLA tissue-engineered scaffolds. J Orthop Surg Res. 2022;17(1):1–17.
68. Guo W, et al. The use of dentin matrix scaffold and dental follicle cells for dentin regeneration. Biomaterials. 2009;30(35):6708–23.
69. Loh QL, Choong C. Three-dimensional scaffolds for tissue engineering applications: role of porosity and pore size. 2013.
70. Zhang K, et al. Advanced smart biomaterials and constructs for hard tissue engineering and regeneration. Bone Res. 2018;6(1):31.
71. Christenson EM, et al. Nanobiomaterial applications in orthopedics. J Orthop Res. 2007;25(1):11–22.
72. Souto-Lopes M, et al. Full physicochemical and biocompatibility characterization of a supercritical CO2 sterilized nano-hydroxyapatite/chitosan biodegradable scaffold for periodontal bone regeneration. Biomaterials Adv. 2023;146:213280.
73. Eshkol-Yogev I, et al. Cell viability of novel composite hydrogels loaded with hydroxyapatite for oral and maxillofacial bone regeneration. Odontology. 2022;110(2):296–304.
74. Dudina DV, Bokhonov BB, Olevsky EA. Fabrication of porous materials by spark plasma sintering: a review. Materials. 2019;12(3):541.
75. Eom J-H, Kim Y-W, Raju S. Processing and properties of macroporous silicon carbide ceramics: a review. J Asian Ceam Soc. 2013;1(3):220–42.
76. Nikolova MP, Chavali MS. Recent advances in biomaterials for 3D scaffolds: a review. Bioactive Mater. 2019;4:271–92.
77. Bahraminasab M et al. On the manufacture of a porous alumina-titanium biocomposite by spark plasma sintering. Mater Chem Phys, 2022;280:125831.
78. Bahraminasab M, et al. 3D printed polylactic acid/gelatin-nano-hydroxyapatite/platelet-rich plasma scaffold for critical-sized skull defect regeneration. Biomed Eng Online. 2022;21(1):1–25.
79. Janmohammadi M, et al. Effect of pore characteristics and Alkali Treatment on the Physicochemical and Biological properties of a 3D-Printed Polycaprolactone Bone Scaffold. ACS Omega; 2023.
80. Yahay Z, et al. Fabrication of meso/macroporous TiO2/PCL composite scaffolds by direct ink writing: the effects of porogen content on the compressive modulus and in vitro behavior. Mater Today Commun. 2023;35:105769.
81. Yahay Z, et al. Fabrication of highly ordered willemite/PCL bone scaffolds by 3D printing: nanostructure effects on compressive strength and in vitro behavior. J Mech Behav Biomed Mater. 2023;144:105996.
82. Yahay Z, et al. Evaporation-induced self-assembly of hierarchical zinc silicate hybrid scaffolds for bone tissue engineering: Meso and macro scale porosity design. Ceramics International; 2024.
83. Yahay Z, Mirhadi SM, Tavangarian F. Fabrication and characterization of Willemite scaffolds using corn stalk as a Novel Bio Template for bone tissue Engineering Applications. J Bionic Eng. 2023;20(1):16–29.
84. de Brito Soares AL, Luz EPCG, Vieira RS. Adsorption processes for forming biomaterials of cellulose and hydroxyapatite for applications in bone tissue regeneration. Adsorption, 2024: pp. 1–13.
85. Khajavi S, et al. Design and synthesis of berberine loaded nano-hydroxyapatite/gelatin scaffold for bone cancer treatment. New J Chem. 2024;48(15):6977–96.
86. Gromolak S, et al. Biological characteristics and osteogenic differentiation of ovine bone marrow derived mesenchymal stem cells stimulated with FGF-2 and BMP-2. Int J Mol Sci. 2020;21(24):9726.
87. Hatakeyama W, et al. Effects of apatite particle size in two apatite/collagen composites on the osteogenic differentiation profile of osteoblastic cells. Int J Mol Med. 2013;32(6):1255–61.
88. Dacic S, et al. Col1a1-driven transgenic markers of osteoblast lineage progression. J Bone Miner Res. 2001;16(7):1228–36.
89. Liu TM, Lee EH. Transcriptional regulatory cascades in Runx2-dependent bone development. Tissue Eng Part B: Reviews. 2013;19(3):254–63.
90. Jeon E et al. Investigating the role of FGF18 in the cultivation and osteogenic differentiation of mesenchymal stem cells. 2012.
91. Yiğiter Ö, et al. The effects of type I collagen on bone defects and gene expression changes for osteogenesis: in a rat model. J Cell Biochem. 2019;120(7):11525–30.
92. Hu K, Olsen BR. The roles of vascular endothelial growth factor in bone repair and regeneration. Bone. 2016;91:30–8.
93. Mirjalili F, Kafashiyan A, Salahi E. The effect of MgCl2. 6H2O and NaF on properties of Chitosan/HAAl2O3 Scaffold. J Nanoanalysis. 2021;8(2):135–44.
94. Zijah V, et al. Towards optimization of odonto/osteogenic bioengineering: in vitro comparison of simvastatin, sodium fluoride, melanocyte-stimulating hormone. Vitro Cell Dev Biology-Animal. 2017;53(6):502–12.

Publisher's note